Combination of Cu-Pt-Pd nanoparticles supported on graphene nanoribbons decorating the surface of TiO_2 nanotube applied for CO_2 photoelectrochemical reduction

Marciélli Karoline Rodrigues de Souza[a]; Eduardo dos Santos Freitas Cardoso[a]; Guilherme V. Fortunato[b]; Marcos R.V. Lanza[b]; Carlos Eduardo Nazário[a]; Maria Valnice Boldrin Zanoni[c]; Gilberto Maia[a]; and Juliano Carvalho Cardoso[a]

[a] Institute of Chemistry, Federal University of Mato Grosso do Sul, Av. Senador Filinto Muller, 1555, CP 549, CEP 79074-460, Campo Grande, MS, Brazil

[b] São Carlos Institute of Chemistry, University of São Paulo, Av. Trabalhador São-Carlense 400, São Carlos, SP 13566-590, Brazil

[c] São Paulo State University (UNESP), Institute of Chemistry, Araraquara, São Paulo, Brazil

Abstract

The photoelectrocatalysis (PEC) technique was applied in CO_2 reduction using different proportions of Cu, Pd, and Pt supported on graphene nanoribbons (GNR) and deposited on the surfaces of TiO_2 nanotubes. Altogether, nine combinations of TiO_2-NT/GNR-metal were assembled, although only three of them efficiently promoted the generation of methanol and ethanol in high quantities. Comparison with the photocatalysis, photolysis, and electrocatalysis techniques showed the extremely high efficiency of PEC, which enabled production of methanol and ethanol at levels around 19.2-fold and 44.4-fold higher, respectively, than photocatalysis, the second most efficient technique. The presence of metallic nanoparticles in the system facilitated CO_2 reduction due to the trapping of the photogenerated electrons, prolonging their lifetime, lowering the reaction energy barrier for CO_2 reduction, and provided active intermediates. Therefore, the assembly of these materials containing low amounts of metals is highly promising, since it can assist in alleviating environmental problems caused by CO_2 emissions, while at the same time enabling the energetically efficient generation of compounds of commercial value.

Keywords: Photoelectrocatalysis; photocatalysis; added-value products; methanol; ethanol.

Introduction

The use of the fossil matrix as a source of energy is responsible for one of the fastest and most intense changes in human society in the history of the planet. Concomitantly, there has been a gradual but steady increase in the concentrations of gases that alter the energy balance of the terrestrial atmosphere [1–3]. Consequently, there is an increasing demand for sustainable energy sources and processes that cause low damage to the environment, especially considering the issue of global warming. There are many alternatives to the current problematic energy model. Among them can be highlighted the reuse of emitted anthropogenic carbon dioxide, which is the main contributor to the greenhouse effect and global warming [4–6].

Therefore, reducing CO_2 emissions into the atmosphere has become a critical issue and various solutions have been proposed in the literature [3,7]. Considering the economic aspects, the use of techniques mimicking the photosynthetic system appears to be a viable option. Among them, the photochemical and photoelectrochemical reduction of CO_2 is a promising approach for the production of fuels, which could potentially reduce the dependence on fossil fuels and mitigate CO_2 emissions to the atmosphere [6,8], with the generation of high added-value compounds.

Photocatalytic and photoelectrocatalytic processes are based on photoexcitation by light without or with application of an external bias potential, respectively [9]. During the process, hole-electron pairs are photogenerated and separated at the semiconductor/electrolyte interface, which can be exploited in a multiple reaction leading to various products and water. The reduction of CO_2 by photogenerated electrons in each of these paths to a specific product can be described as one of many competing reactions [10–13]. The overall reactions involve a series of intermediate steps, each with competing reactions, with progress depending on the metal catalyst, the electrolyte, and several other factors [14–16]. The photocatalyst plays an important role in photocatalysis/photoelectrocatalysis, with the selectivity of the products formed depending on parameters such as temperature, pressure, pH, applied potential, and the adsorption/desorption properties of the CO_2 and intermediates on the semiconductor surface [17,18].

The use of the TiO_2 semiconductor in the photocatalytic reduction of CO_2 has attracted the attention of researchers, due to its photostability, non-toxicity, chemical stability, and low cost [2,7]. Modification of the TiO_2 surface with metals, non-metals, and other semiconductors offers promising ways to improve electrode performance

[2,19–23]. Graphene derivatives such as graphene oxide, reduced graphene oxide, and their functionalized forms are attractive components for use in optoelectronic device fabrication, due to their unique optical, thermal, mechanical, and electrochemical properties [15,24–28]. In particular, the 2D carbon nanostructure has proven to be an excellent candidate for the extraction of solar energy and its chemical transformation to fuel by photocatalytic water splitting and CO_2 conversion [29,30]. Among carbon nanostructures, graphene nanoribbons (GNRs) from multiwalled carbon nanotubes (MWCNTs) demonstrated remarkable enhancements in catalytic activity, due to their unique properties [31,32]. Generally, graphene has a two dimensional (2D) planar geometry with sp2 character (π electronic cloud), a single layer of carbon atoms with outstanding charge mobility, thermal conductivity, high surface area, and zero band gap energy [31,32]. Due to the high redox activity of crystalline defects in 2D carbon structures, the graphene hybridized light absorber antenna has been the subject of photoelectrochemical research [15,33].

The photocatalytic activity of TiO_2 with graphene oxide incorporated in its structure has been studied [34]. The photoelectrocatalytic reduction of CO_2 at Cu-doped TiO_2 supported on reduced graphene oxide resulted in the formation of methanol and formic acid, when CO_2 was dissolved in aqueous 10% methyl diethanolamine (MDEA) solution [35]. Investigation of the photoelectrocatalytic performance of TiO_2 nanotubes decorated with Pt NPs supported on rGO and deposited on a conductive Cu foam separated by a Nafion membrane found that CO_2 was converted to formic acid, methanol, propionic acid, and other products [36]. Studies with graphene deposits on ZnO/rGO composite have also described the reduction of CO_2 to methanol [37]. These investigations have indicated that the incorporation of rGO on the semiconductor surface can improve electron transfer from the semiconductor to the adsorbed CO_2, as well as reduce the rate of recombination of the photogenerated electrons and holes. Several reports highlighted the combination of carbon nanomaterials with metallic nanomaterials to improve the CO_2 catalytic properties while reducing the metal loading [38,39]. The synergistic effects derived from a combination of two or more elements may alter the electronic structure with d-band shift, surface defects and surface-lattice strain, differentiating the energy barrier required for CO_2 activation as well as the binding energies to radical species [40].

The specificity towards the products formed remains a challenge, with few catalysts being able to resolve this issue. However, there are some characteristic products for the photoelectrocatalytic reduction of CO_2 on the surfaces of different metals, such as carbon monoxide for platinum, formic acid and H_2 for palladium, and hydrocarbons and other carbonaceous species for copper [41]. In this way, synthesizing materials with low amounts of these elements but maintaining the efficiency of the process is a challenge. The noble metal-based electrocatalysts remain the top priority in relevant industrial applications in despite of the scarcity and high cost [42].

Hence, the use of these metals in different combinations, anchored on the surface of GNRs and deposited on TiO_2 nanotubes, can provide photocatalytic reduction of CO_2, with different products generated on the surface of each metal. This approach, taking advantage of the properties of GNRs, can increase and diversify the generation of compounds in this reaction. Therefore, the main objective of this work was to manufacture electrodes using different combinations of copper, palladium, and platinum anchored on GNRs, with these nanostructures being deposited on the surface of TiO_2 nanotubes. An experimental analysis obtained from these different combinations will be discussed in terms of the most efficient materials for CO_2 photoconversion. The materials obtained were then used in the photoelectrocatalytic reduction of CO_2.

Methodology

TiO_2 nanotubes

TiO_2 nanotubular materials were prepared as described by Cardoso [43–48]. Titanium plates (Realum, 99%) were cut (6.6 cm^2) and subjected to rigorous mechanical tinning using different grades of sandpaper. They were then submitted to ultrasonication in acetone, isopropanol, and deionized water, for 15 min each, followed by drying in an N_2 atmosphere. The electrolyte used for the formation of the nanotubes consisted of glycerol:water solution (90%:10%) containing 0.25% NH_4F. The plates were anodized in a sealed reactor with capacity of 200 mL, where the titanium plate (anode) was positioned 1 cm away from a DeNora® DSA plate (cathode). A voltage of 30 V (2.0 V/minute) was applied to this system, maintained for 50 h. After this process, the plates were washed with deionized water, dried under N_2, and subjected to calcination at a temperature of 450 ºC for 2 h, with a heating ramp of 2 ºC min^{-1}.

Preparation of GNRs

The procedure described by Lima and Maia [31] was used to prepare the GNRs from MWCNTs (10 ± 1 nm o.d. × 4.5 ± 0.5 nm i.d. × 3-6 μm length, 6-8 nm tube walls; Aldrich). The physical aspects and surface characteristics of the GNRs can be found in a previous report [31].

Preparation of GNR-metal nanoparticles

The depositions of metallic nanoparticles (Cu, Pt, and Pt) were performed as described by Boone and Maia [32]. Table S1 shows the masses and proportions of the compounds used for preparation of the samples. The syntheses were performed in sealed glassware, under an N_2 atmosphere. Previously defined masses were solubilized in 25 mL of deionized water together with 24.4 mg of Pluronic F-127 surfactant (Sigma Aldrich), with ultrasonication for 40 min. The solution was then submitted to carefully controlled heating to 80 ºC. After reaching this temperature, 1.0 mL of ascorbic acid solution (0.0835 mol L^{-1} for samples S01 and S03-S09, and 0.0417 mol L^{-1} for samples S02) was added, followed by agitation for 2 h. After this period, the samples were cooled to room temperature, centrifuged, and subjected to a continuous washing process to remove the surfactant. Finally, the materials were dried in an oven at 30 ºC and stored in sealed tubes kept in a desiccator.

Deposition of GNR-metal nanoparticles on TiO_2 nanotubes

The deposition of the GNR-metal nanoparticles was performed by the drop coating technique, where each prepared material was dispersed in 2.0 mL of deionized water to obtain a load condition of 150 μg cm^{-2} and a concentration of 0.5 μg mL^{-1}. After preparing this mixture, it was dispensed onto the surfaces of the TiO_2 nanotubes and evaporated at room temperature.

CO_2 reduction

The CO_2 reduction experiments were carried out in a 200 mL stainless steel reactor (130 mL for solution and 70 mL headspace) (Fig. S1). A quartz glass (3 mm thickness and area of 35 cm^2) was positioned at a distance of 5 mm from the bare and modified TiO_2 nanotube samples. A 0.1 mol L^{-1} solution of sodium sulfate (pH 6.4) was initially saturated by bubbling CO_2 gas (99.0%, White Martins) for 30 min, at a flow rate of 1.0 mL min^{-1}. This solution was then transferred to the reactor and left under 1.0 atm of CO_2

gas pressure to maintain saturation of the system. Activation of the photocatalysts was performed using an Oriel solar simulator fitted with a 150 W Xe lamp. For the photocatalytic experiments, only the photocatalysts were employed in the system, while for photoelectroreduction, a constant potential was applied using a potentiostat/galvanostat (Model 128N, Autolab) with an Ag/AgCl (3.0 mol L^{-1} KCl) reference electrode and a DeNora DSA (8.0 cm^2) counter electrode. Aliquots were removed at preestablished times and stored in sealed vials, under refrigeration, until analysis. All the experiments were performed in triplicate.

Product identification

The products formed after CO_2 reduction were identified and quantified by gas chromatography with flame ionization detection (GC-FID), using a Shimadzu Model 2010 instrument coupled to an automatic detector (CombPal). An RTX-1 column (30 m × 0.32 mm, 0.30 µm) was used, with an isothermal temperature of 50 ºC and helium as the carrier gas at a constant flow rate of 1.9 mL min^{-1}. The analyses were performed using the headspace extraction method for liquid samples. For this, a 2.0 mL aliquot of the sample was transferred to a sealed 10 mL vial, followed by heating to 76 ºC and keeping under incubation for 5 min, with agitation at 250 rpm (using cycles of agitation for 5 s and pause for 2 s). At the end of this heating, a 500 µL volume of the headspace gas was collected and injected into the chromatographic system, with an injector temperature of 150 ºC and split condition of 5:0. All the analysis conditions are provided in Table S2. The limits of quantification were calculated, and the values were obtained: 14.62 µmol L^{-1} for methanol and 11.41 µmol L^{-1} for ethanol, while the detection limits were 4.82 µmol L^{-1} for methanol and 3.76 µmol L^{-1} for ethanol.

Characterization procedures

The material characterization by transmission electron microscopy (TEM), scanning-TEM (STEM), and elemental identification using energy-dispersive X-ray spectroscopy (EDX) were carried out using a FEI TECNAI G^2 F20 HRTEM microscope at 200 kV. The samples were prepared from an ethanolic dispersion containing the catalyst film which were carefully removed from the titanium electrode plate. Subsequently, 3 µL of the dispersion was dripped onto a lacey carbon film (300-mesh) on a Cu TEM grid.

The catalyst surface chemistry characterization by X-ray photoelectron spectroscopy (XPS) was performed out using an Omicron surface analysis station coupled to a SPHERA hemispherical analyzer and a DAR 400 Al K_α x-ray source ($h\nu$ = 1486.7 eV). The binding energy scales were calibrated based on the C-C contribution of carbon 1s peak at 284.8 eV. The quantification of Ti, C, N, O, Cu, Pd, and Pt was estimated from the relative peak area proportions considering the Scofield atomic sensitivity factors [49].

Field emission gun scanning electron microscopy (FEG-SEM), using a JEOL 7500F microscope, was employed to analyze the morphologies of the tubular TiO_2 nanostructures with and without the presence of GNR-metal.

Evaluation of the photoactivity of the electrodes and the photoelectrolysis employed an Autolab PGSTAT 128N potentiostat/galvanostat controlled with NOVA 1.10 software. The photocurrent was measured by linear scanning voltammetry.

An Agilent Cary 60 UV-Vis spectrophotometer was used to measure the diffuse reflectance spectra of the materials and to calculate the band gap of the catalyst. Tauc graphs were used to estimate the band gap energies of the materials. This method consists of extrapolating the linear portion of a plot of $\alpha(h\upsilon)^{1/\gamma}$ as a function of $h\upsilon$ (eV), where the intercept at $\alpha = 0$ is the optical band gap (E_{bg}, in eV). In these expressions, α is the absorption coefficient, h is Planck’s constant (J s), υ is the frequency (s^{-1}), and γ is the power coefficient, whose values can be 1/2, 3/2, 2, or 3, depending on the type of electronic transition: direct allowed, direct forbidden, indirect allowed, and indirect forbidden, respectively. The diffuse reflectance measurements were converted to equivalent absorption coefficients, using the Kubelka-Munk (K-M) method.

Thermogravimetric analyses were carried out using a Shimadzu GA-50 instrument, with samples (2-5 mg) placed in alumina crucibles and heated from 25 to 900 ºC, at a rate of 10 ºC min^{-1}, under a flow of synthetic air (5.0 FID, 50 mL min^{-1}).

Results and discussion

The photoelectrocatalytic reduction of CO_2 employing the nine combinations TiO_2-NT/GNR-M was performed obtaining as products in higher quantity, methanol and ethanol. Table S3 shows the respective quantities for these initial analyzes.

As noted, of all these combinations, only the catalysts, S01, S02 and S08 promoted the photoreduction of CO_2 in values above of the limit of quantification defined by the identification method and, therefore, only these were submitted for the characterizations.

The conditions that influence CO_2 reduction performance will be discussed in the subsequent topics.

Characterization of photocatalysts

STEM, TEM, and HR-TEM analyses

Figure 1 shows the STEM and TEM images for the S01, S02 and S08 photocatalyst samples. The STEM image for the S01 catalyst shows the GNR/Cu nanocomposite very close to the TiO_2 nanotubes (NT) and the presence of small Cu nanoparticles (~10 nm on average) widely dispersed on the GNR. TEM and HR-TEM images clearly show the high proximity between GNR/Cu nanocomposite and TiO_2 structures. The images also reveal the presence of clear crystalline pattern of TiO_2 NT and Cu nanoparticles (NP), e.g., the *d*-spacing with average values of 0.482, 0.342, and 0.207 nm; which are typically expected for planes (0 0 2) and (1 0 1) of anatase phase of TiO_2 (JCPDS 21-1272); and (1 1 1) of face-centered cubic (fcc) crystalline Cu systems (JCPDS 71-4610), respectively. In STEM image recorded for the S02 catalyst (c.f. Fig. 1) can be observed the presence of rough Pt-Pd-Cu nanoparticles with not well-defined shape and sizes of around 60 nm; which are dispersed on the GNR. The image also suggests the presence of agglomerates in some regions, these observations are in line with previous reports [32,50]. TEM and HR-TEM images for the S02 catalyst clearly show the GNR/Pt-Pd-Cu nanocomposite in contact with the TiO_2 NT, as well as the crystalline features for both structures evinced by the *d*-spacing values of 0.342, 0.225, and 0.198 nm; which are expected for the planes (1 0 1) of anatase phase; and (1 1 1) and (1 0 0) of *fcc* crystalline Pd or Pt systems [50–52], respectively. The STEM image for the S08 catalyst exhibits the presence of star-like shaped Pt-Pd-Cu NPs with sizes of around 30 nm which can be found in highly dispersed way on the GNR. Similarly to S02 sample, TEM and HR-TEM images for the S08 catalyst sample show the GNR/Pt-Pd-Cu nanocomposite close to the TiO_2 NT, as well as the *d*-spacing with values of 0.223, and 0.198 nm, which are related to planes (1 1 1) and (1 0 0) of *fcc* crystalline Pd or Pt systems [50–52], respectively. The Elemental EDX-mapping images for the S08 catalyst (Figure S2) show that Pt, Pd, and Cu, are well distributed on the GNR, suggesting that the three metals are forming an alloy, which is in line with other previously reported results for Pt-Pd-Cu/GNR nanocomposite [32,50].

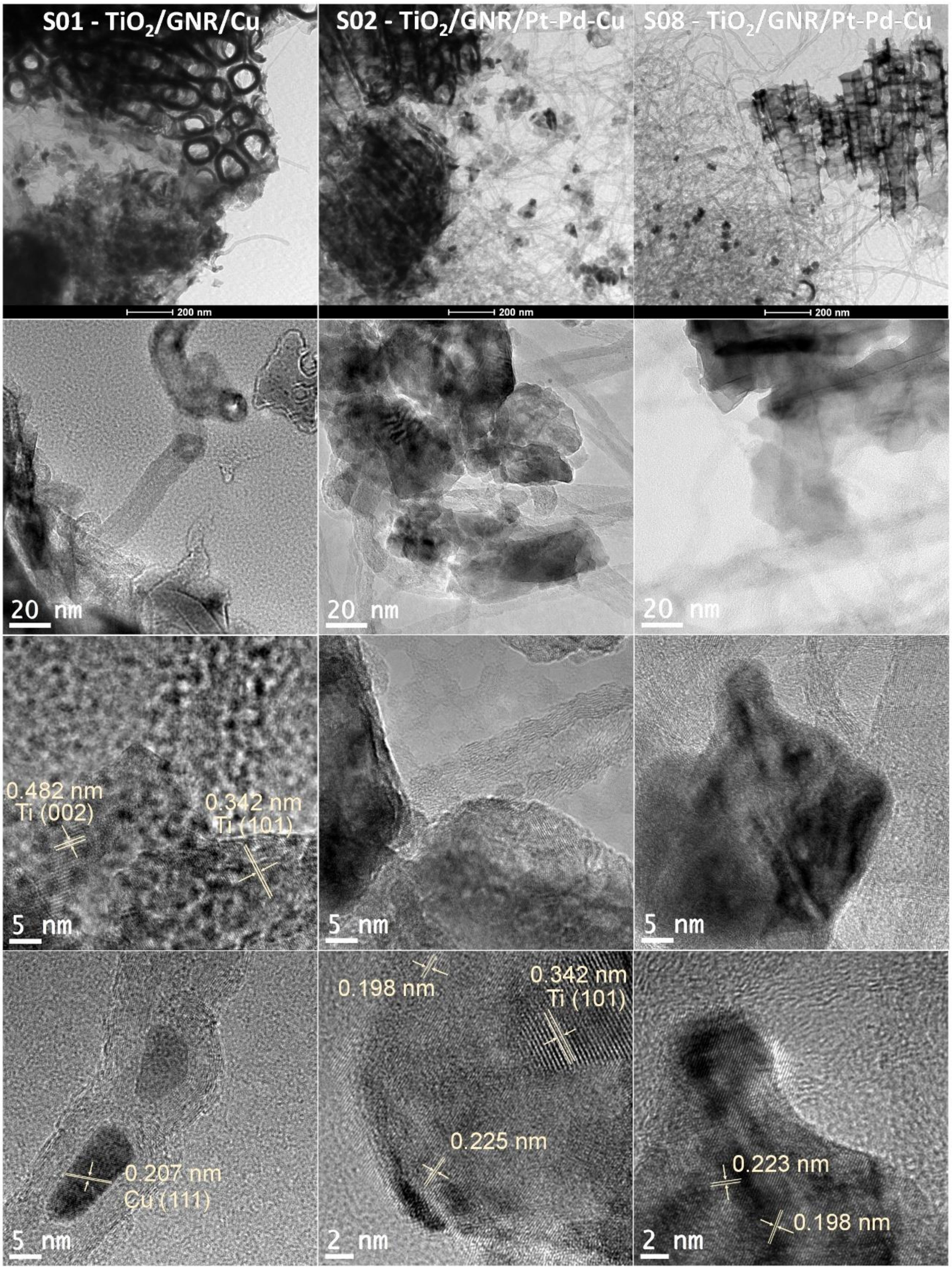

Figure 1. Representative BF-STEM (first row), TEM (second row), and HR-TEM (third and four rows) images for the S01, S02, and S08 samples.

FEG-SEM analysis

Fig. 2A shows scanning electron microscopy (FEG-SEM**)** images of the S01, S02, S07, and S08 photocatalysts, chosen as representative materials and prepared as described previously. There was a clear distribution of graphene nanoribbons across the surfaces of the TiO_2 nanotubes, without total blockage of the semiconductor. Thin films are important to keep the TiO_2 nanotubes easily photoexcited by light, initiating the generation of charge carriers and favoring the electronic transfer processes. Although the acquisition of the images using the secondary electron capture (SEI) mode did not enable identification of the metallic nanoparticles on the GNR with good resolution, this was improved by changing the image capture mode to the backscatter condition (BSE), as shown in Fig. 2B. The results showed metallic nanoparticles present on the TiO_2 nanotube surfaces, except for photocatalyst S07, which only showed the presence of GNRs. Sample S01 showed nanoparticles with diameters of around 5-20 nm dispersed in several regions on the GNRs, while samples S02 and S08 showed agglomerates of nanoparticles around 30-80 nm in size. These features corroborated the results of the scanning electron microscopy/energy dispersive X-ray spectrometry (SEM/EDX) assays (Fig. 2C), which showed the presence of all the elements used in the syntheses of the corresponding materials.

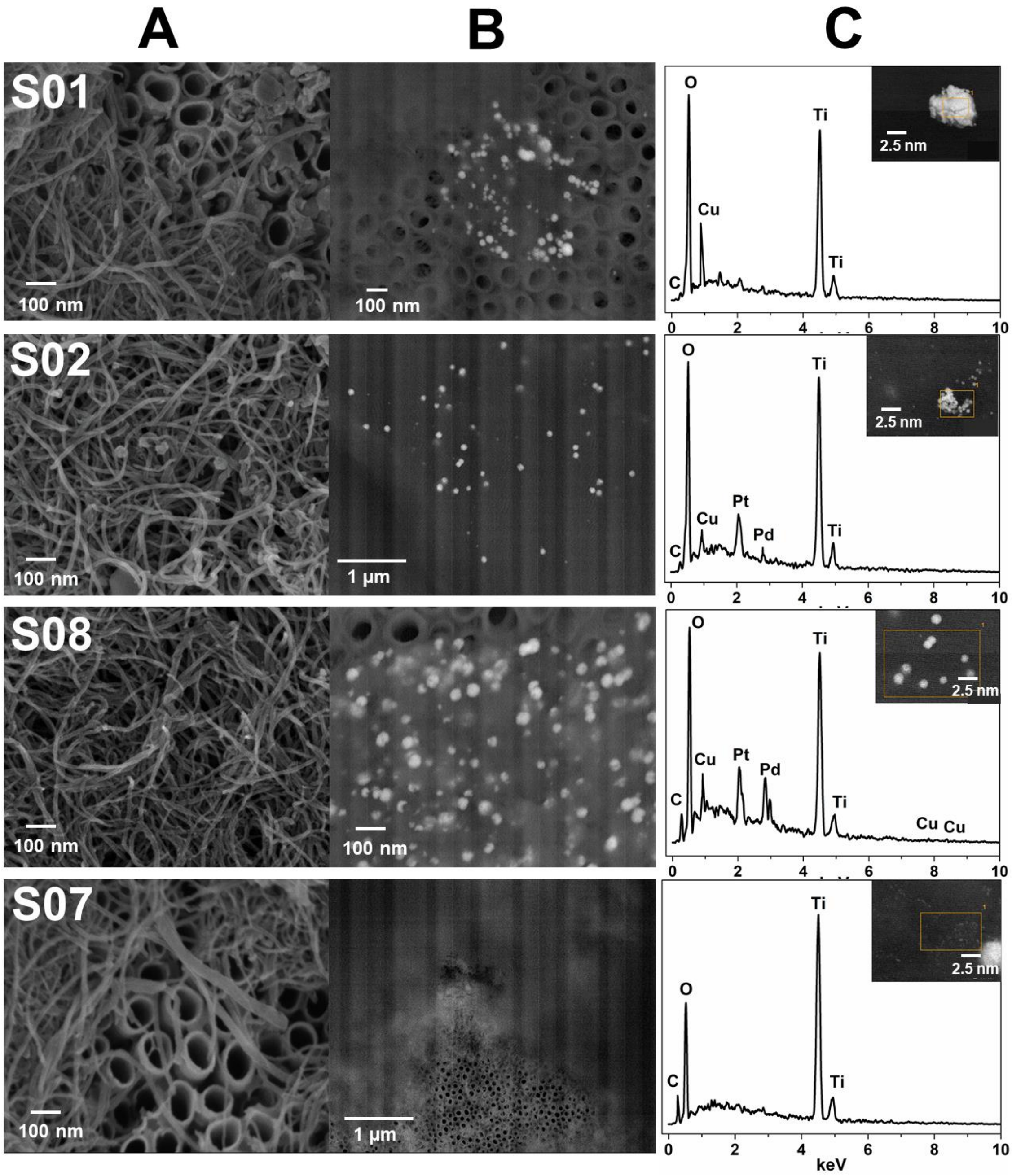

Figure 2. Scanning electron microscopy images of samples S01, S02, S08, and S07, using (A) secondary electron mode (SEI) and (B) backscattered electron mode (BSE). (C) Results of scanning electron microscopy/energy dispersive X-ray spectrometry (SEM/EDX) analyses of the materials.

XPS analysis

The XPS survey spectra for the S01, S02, S07, and S08 catalyst samples are shown in Figure S3. For all samples can observed the presence of peaks related to C 1s, O 1s, N 1s, and Ti 2p at around 283.9, 531.9, 399.9, and 457.9 eV, respectively (c.f. Table S4). The peak associated to the Cu 2p can be found at 933.9 eV for S01, S02, and S08 catalyst, while the not well-visible peaks related to Pt 4f and Pd 3d at around 72.9 and 338.0 eV, respectively, can be found only for S02, and S08 samples. Table S4 lists the elemental quantification roughly estimated by XPS survey spectra. The Cu content in S01 was found to be 2.1 wt.%, while the content of Cu, Pt, and Pd in S02 and S08 catalysts were found to be relatively close to the EDX and TGA results, with values of Cu-0.4, Pt-1.1, and Pd-0.55 wt.% for the S02 sample and Cu-0.4, Pt-0.7, and Pd-1.7 wt.% for S08 sample (c.f. Tables 1 and S4). The enrichment with a specific element may affect reaction mechanisms as well as the nature of the reaction products [53].

Figures S4 shows the high resolution XPS (HR-XPS) spectra in the C 1s, O 1s, and N 1s regions for the S01, S02, S07, and S08 photocatalyst samples. In general, the HR-XPS spectra in the C 1s and N 1s exhibited similar features for all samples; which were deconvoluted into the peaks C–C (284.9 eV on average), C–H (284.6 eV), C–O (286.6 eV), C=O (~87.9 eV), and O–C=O (289.2 eV) for C groups; pyridinic-N (399.1 eV), pyrrolic-N (400.2 eV), graphitic-N (401.1 eV), and oxidized-N (402.5 eV) for N groups. These results are in good agreement with previous reports [50,54–56] involving GNR (c.f. Table S5). The O 1s HR-XPS spectra were deconvoluted in three main peaks which are attributed to the groups TiO_2 (530.8 eV), O–C/O=C (533.1 eV), and O–C=O (534.9 eV). The samples that contains Pd and Pt metals in their compositions were additionally deconvoluted into the peaks PdO (531.1 eV) and $Pt(OH)_2/PtO_2$ (531.7 eV) [50]. The percentage content for the deconvoluted groups can be found in Table S5 and are in good agreement with other previously published reports [50,54–56].

In the HR-XPS spectra for Ti 2p region (Figure S5) can be found the presence of Ti $2p_{3/2}$ and Ti $2p_{3/2}$ peak couples, which were deconvoluted into three doublet peaks associated to the following groups: Ti^{2+} (455.1 and 462.5 eV), Ti^{3+} (457.0 and 463.1 eV), and TiO_2 (460.0 and 465.7 eV). For all samples, the TiO_2 state represented the highest percentage content with 86.1%; which was found to be in line with other previously reported results for TiO_2 nanotubes [57,58] (c.f. Table S5). The Cu 2p spectra were deconvoluted into three peaks, attributed to the following groups: Cu_2O (~933.4), CuO (~935.2 eV), and Cu(II) shake-up (~941.7 eV). Cu(0) state was not found likely due to the spontaneous oxidation of copper in ambient contained oxygen [59,60]. With regard to % content (c.f. Table S5), S02 sample exhibited the largest content of Cu_2O (45.6 %) in comparison with S01 (24.9 %) and S08 samples (18.3 %). It is worth noting that the Cu(I) presence on the catalyst has been reported to impact positively the catalytic activity on CO_2 reduction reaction [26,61–63]. The Pt 4f XPS spectra were deconvoluted into three peak couples which can be ascribed to the spin-orbit split $4f_{7/2}$ and $4f_{5/2}$ peaks for Pt(0) (69.7 and 74.2 eV), PtO (71.7 and 75.6 eV), and PtO_2 (73.5 and 76.7 eV) (c.f. Table S5) [50]. With regard to the percentage content, S02 catalyst sample exhibited 20.3% of Pt(0), 48.4% of PtO, and 31.3% of PtO_2, while the S08 sample demonstrated the values of 18.9%, 24.2%, and 56.9% (Table S5) [50]. Finally, the XPS spectra in the Pd 3d region could be deconvoluted into three peak couples typically associated to the spin-orbit split $3d_{5/2}$ and $3d_{3/2}$ peaks for the Pd(0) (333.6 and 340.6 eV), PdO (336.4 and 341.4 eV), and PdO_2 (338.7 and 344.0 eV) groups [50]. For the S02 catalyst sample, the percentage content of the Pd states were found to be as following: Pd(0) 20.4%, PdO 17.0%, and PdO_2 62.6%. For the S08 catalyst, the content of Pd(0) was found to be 14.8%, PdO 12.1%, and PdO_2 73.1%. Although slight displacements (~0.5 eV) of the binding energy positions for the Pt and Pd groups to S02 in relation to S08 catalyst have been detected, the very low signal-to-noise ratio of the Pd 3d and Pt 4f spectra (which is due to the low content of these metals in the samples) precludes further conclusions in this direction.

Thermogravimetric analysis

Figure 3 shows the thermogravimetric curves obtained for the GNR and GNR-M samples. The presence of metals incorporated in the GNR structure lowered the temperature required for complete combustion of the material [32]. For S07, this occurred at approximately 592 ºC (curve A), while the corresponding temperatures were 510 ºC for S01 (curve B), 504 ºC for S02 (curve C), and 562 ºC for S08 (curve D).

Quantification of the incorporated metals was performed by the combination of thermogravimetric and energy dispersive X-ray spectroscopy (EDX) analyses. The results (Table 1) revealed slight differences after deposition of the metals, relative to the initial values. This may have been due to metals that were poorly adsorbed on the surface of the GNR or had been removed in the washing process (post-synthesis). Table S6 details how these values were obtained.

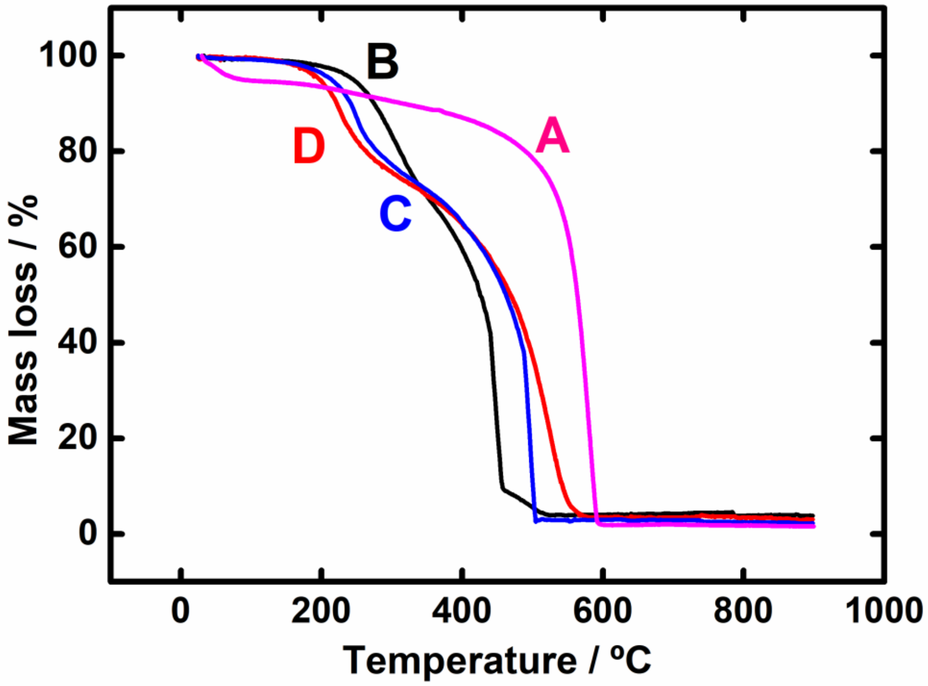

Figure 3. Thermal decomposition behaviors of (A) S07, (B) S01, (C) S02, and (D) S08.

Table 1. Experimental values (weight %) obtained for the elemental compositions of the S01, S02, S08, and S07 materials, based on the masses remaining unburned after the TG analyses (Figure 3) and the metals detected in the EDX analyses (Figure 2).

Synthesized material	**Elements (weight %)**			
	C + O + N + H	**Pt**	**Pd**	**Cu**
S01	95.9	-	-	4.1
S02	97.5	1.2	0.6	0.7
S08	96.7	0.6	2.1	0.6
S07	98.3 [32]. Other = 1.7 [32]	-	-	-

UV-Vis analysis

Figure 4 compares the UV-Vis absorption spectra obtained for the electrode samples synthesized. A slight increase in the UV absorption at 390 nm was observed for the electrode modified with GNR, compared to the bare TiO_2 nanotube electrode. The incorporation of metals on the surfaces of the new materials resulted in significant increases of absorption at 390 nm, of 2.77x for S01, 2.89x for S02, and 2.74x for S08.

The estimated band gap values (Fig. S5) obtained from these spectra and the Kubelka-Munk equation were 3.33 eV (TiO_2-NT), 3.19 eV (S07), 3.10 eV (S01), 3.13 eV (S02), and 3.01 eV (S08). Hence, it was evident that the material could also be photoactivated in the visible spectral region, which could increase the efficiency of the photocatalytic/photoelectrocatalytic process.

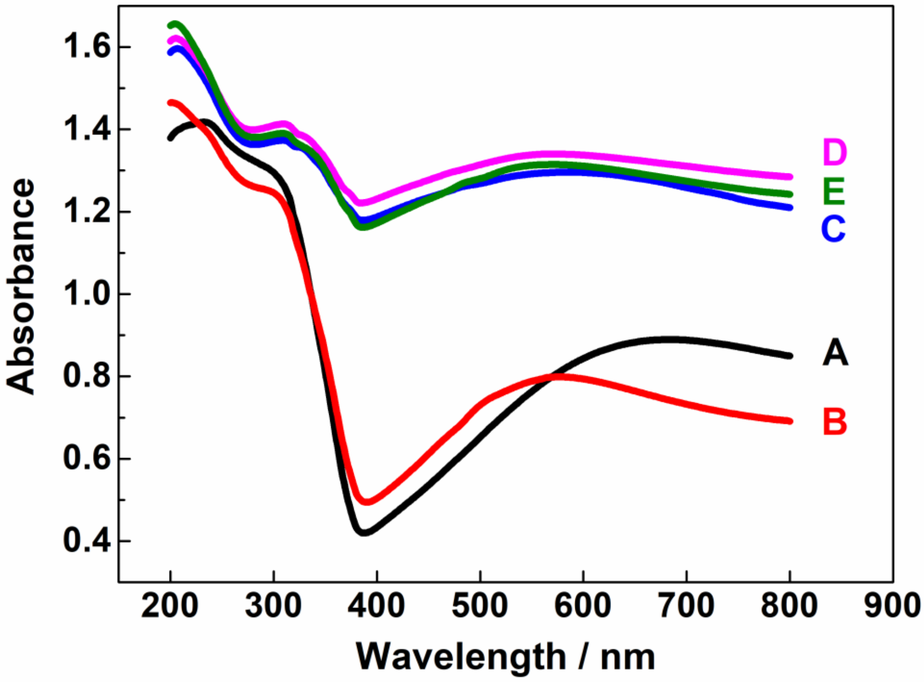

Figure 4. Absorption spectra as a function of wavelength by DRS analysis of (A) TiO_2 nanotubes, (B) S07, (C) S01, (D) S02, and (E) S08.

Photoelectrochemistry

Fig. 5 presents the linear scanning voltammograms for the different syntheses of GNR-M deposited on the surface of TiO_2-NT. As expected, in the absence of illumination, no photocurrent was generated during the entire potential scan, for any of the materials evaluated (representative curve A). This could be explained by the fact that TiO_2 is an n-type semiconductor and needs to be illuminated at a specific wavelength in order to generate electron/hole charge carriers [43,45,66]. However, when activation of the surface was initiated with light of higher energy than the band gap (3.33 eV), the charge carriers were formed instantly. When the potential value during the scan approaches the flat band potential (E_{fb} for Ti/TiO_2, under these conditions, is around

-0.35 V vs. Ag/AgCl), the phenomenon of band bending (valence and conduction bands) occurs, with the photogenerated holes being directed to the surface of the material, while the trajectories of the electrons are forced towards the interior [9,45,66]. Hence, the curve for the TiO_2 nanotubes (curve B) showed a higher photocurrent, compared to the other photocatalysts. When the GNRs were deposited on the surfaces of the nanotubes, the photogenerated current showed a drastic reduction of around 60.0%, while decreases of 79.3%, 82.8%, and 88.2% were observed for S01, S02, and S08, respectively. This behavior could be explained by two factors: (i) Partial blockage of the surfaces of the TiO_2 nanotubes by the GNRs, as shown in the SEM images (Fig. 2), resulted in a smaller amount of light available to activate TiO_2, so there was lower generation of charge carriers. However, it should be noted that the increased absorption capacity of TiO_2 when the GNRs were present was probably due to an internal filter effect of a few or multiple sheets of layered GNRs. In this case, the photocatalytic activity should not be increased, but rather be decreased, because the photons were not actually absorbed by TiO_2 [15]; (ii) Most of the photogenerated electrons were trapped at the surfaces of the photocatalysts, attracted by the GNRs and the metallic nanoparticles, so fewer charges were forced to the counter electrode, causing a decrease of the photocurrent. This last explanation was coherent with the desired system for reduction of CO_2 and corroborate the results obtained and which will be presented below.

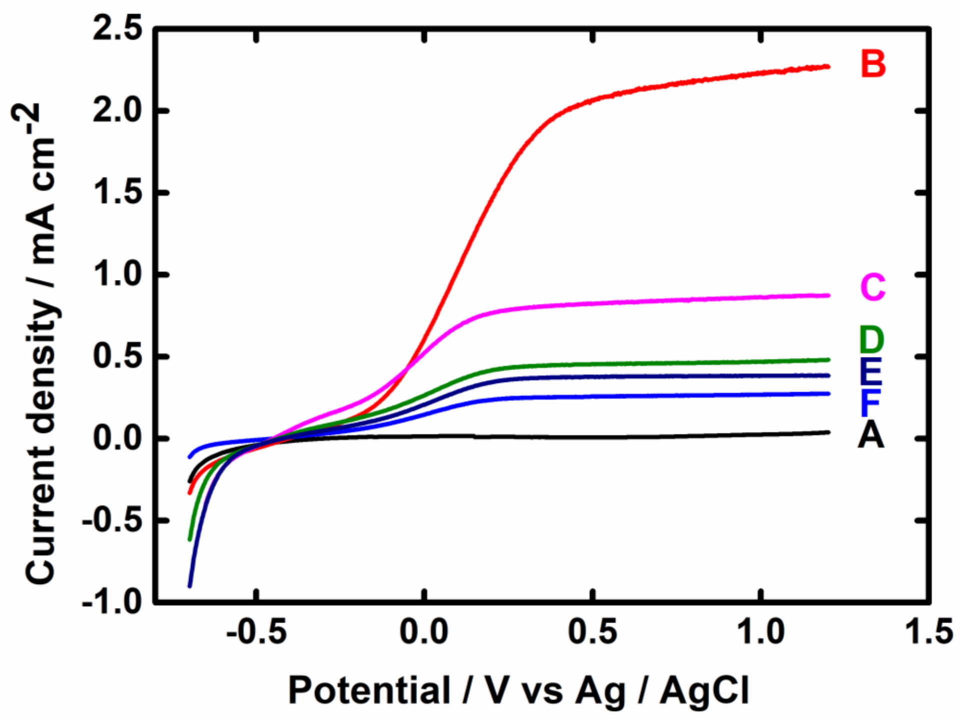

Figure 5. Linear scanning voltammograms for the different electrodes: (A) S08 in the dark, (B) TiO_2 nanotubes, (C) S07, (D) S01, (E) S02, and (F) S08. Conditions: $\upsilon = 10$ mV s^{-1}; 0.1 mol L^{-1} Na_2SO_4; pH 6.4; illumination using a 150 W xenon lamp.

CO_2 reduction

The photoelectrocatalytic reduction of CO_2 was firstly performed using 0.1 mol L^{-1} Na_2SO_4 solution (pH 6.4) saturated with CO_2 for 30 min and pressurized at 1 atm to maintain saturation of the medium. The amounts of the main products formed from this reaction are shown in Fig. 6.

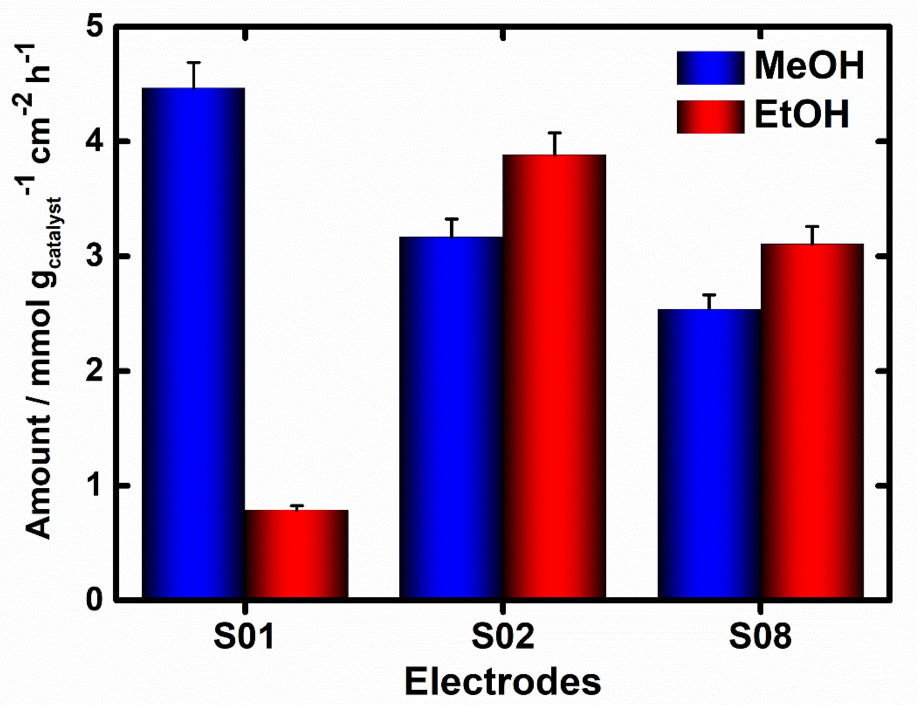

Figure 6. Amounts of methanol (blue columns) and ethanol (red columns) generated by the photoelectrocatalytic process using the S01, S02, and S08 electrodes for 1 h, with bias potential of -0.7 V vs. Ag/AgCl, in 0.1 mol L^{-1} Na_2SO_4, at pH 6.4, under illumination from a 150 W xenon lamp.

After 60 min of the experiments, it was possible to identify methanol and ethanol as the main products generated by the photoelectrochemical reduction of CO_2 by applying -0.7 V vs. Ag/AgCl (3.0 mol L^{-1} KCl), using the S01, S02, and S08 materials illuminated by a 150 W Xe lamp. The depositions of different compositions of the metals Cu, Pd, and Pt on the GNRs were also evaluated using the same experimental protocol. The results are shown in Table S3. No product was identified in the absence of CO_2 (data not shown).

From these results, it was observed that for the materials S03 (TiO_2-NT/GNR/Cu-Pd), S04 (TiO_2-NT/GNR/Cu-Pt), S05 (TiO_2-NT/GNR/Pt) and S09 (TiO_2-NT/GNR/Pt-

Pd) methanol and ethanol were identified, but could not be quantified, since the concentrations were below the quantification limit of the chromatographic methodology. In the case of S06 (TiO_2-NT/GNR/Pd), only ethanol could not be quantified. The S07 sample (TiO_2-NT/GNR) did not promote the formation of any alcohols. This showed that formation of the products could be attributed to the metals deposited on the graphene nanoribbons. In the photoelectrocatalytic system, the GNRs played a fundamental role as the main medium for the deposition of metallic nanoparticles, promoting better transport of electrons to the metals, which, in turn, were principally responsible for the process of CO_2 reduction, while also minimizing the deleterious effects of charge recombination [41,67]. Competitive reactions by these electrons could lead to low performance of the materials, associated with the generation of species such as H_2. The main mechanisms of the generation of products during CO_2 reduction are represented by Equations 1-5.

For the materials S01 (TiO_2-NT/GNR/Cu), S08 (TiO_2-NT/GNR/Cu/Pd-Pt), and S02 (TiO_2-NT/GNR/Cu/Pd-Pt), methanol and ethanol were generated in large quantities. For S01, the generation of methanol was greatly favored by around 5.67x, compared to ethanol, while for S02 and S08, ethanol formation was around 1.23x and 1.22x higher, respectively, compared to methanol formation.

Since the photocatalytic reactions for CO_2 reduction involve the continuous transfer of protons, electrons, and carbon, the number and quantity of products formed depend on the transfer rates of these species and the type of material used in the reaction [68–71]. Previous studies reported in the literature describe the formation of some characteristic compounds generated from the reduction of CO_2 in the presence of metallic co-catalysts, examples being CO for Pt, HCOOH and CO for Pd, and C1-C3 hydrocarbons and other carbonaceous species for Cu [41]. A comparison of these materials revealed that the generation of methanol was greatly favored using S01, which contained a higher quantity of copper (Table 1). In contrast, use of the material with an approximately 2-fold higher content of platinum (S02) favored the formation of ethanol. The same behavior was observed when the material with an approximately 3.5-fold higher content of palladium was used (S08). For these last two cases, it should be highlighted that enrichment with platinum, relative to palladium, slightly favored hydrogenation reactions and the addition of 1 carbon atom to methanol. Hence, the high amounts of alcohol generated in this process could be attributed to effective electronic transfer to the metallic nanoparticles and the respective byproducts formed on their surfaces, with the processes being favored by the aggregation of nanoparticles in clusters (samples S02 and S08). One of the possible pathways for the formation of methanol and ethanol occurs through catalytic hydrogenation processes involving six electrons and six protons (Eq. 4) and twelve electrons and nine water molecules (Eq. 5) throughout the reaction, respectively. This information is summarized in Figure 7.

$2H^+ + 2\,e^- \rightarrow H_{2(g)}$ Eq. (1)

$2H_2O_{(l)} + 4h^+ \rightarrow O_{2(g)} + 4H^+$ Eq. (2)

$CO_{2(g)} + e^- \rightarrow CO_2^-$ Eq. (3)

$CO_{2(g)} + 6H^+ + 6e^- \rightarrow CH_3OH_{(l)} + H_2O_{(l)}$ Eq. (4)

$2CO_{2(g)} + 9H_2O_{(l)} + 12e^- \rightarrow C_2H_5OH_{(l)} + 12OH^-$ Eq. (5)

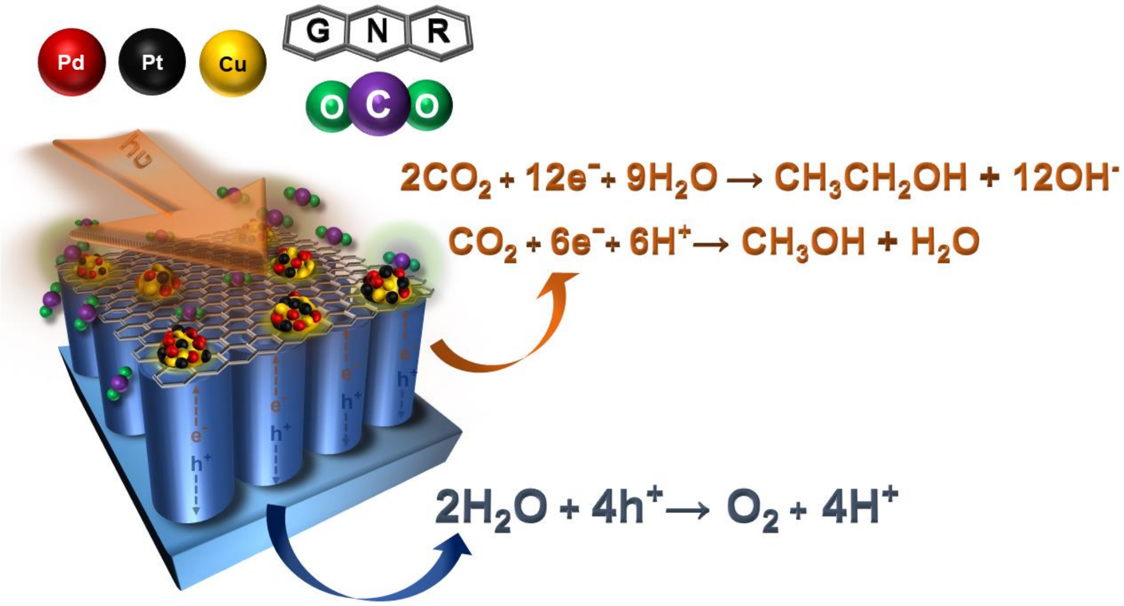

Figure 7. Proposed scheme for the generation of products using the TiO_2-NT/GNR-metal electrodes operated under UV-Vis irradiation.

These results were corroborated by the photocurrent studies (Fig. 5), indicative of separation of the charge carriers and transfer of the photogenerated electrons mainly to the surfaces of the materials, attracted by the metallic nanoparticles [35,72]. The presence of the different metals in the clusters, which was confirmed by TEM, EDX and XPS results (c.f. Figs. 1, 2, S2-5), led to the formation of specific products on the corresponding surfaces, which were rapidly converted to alcohols, due to favoring of the electronic transition associated with the ideal combination within the cluster. This combination suppressed H_2 generation reactions and protected the copper nanoparticles against oxidation, enabling greater conversion to methanol and ethanol.

Importantly, the need to minimize the prevalence of reactions leading to H_2 generation highlighted that the reduction of CO_2 was not governed only by the potential applied to the modified electrodes, since Pt is well known as the best catalyst for electrochemical H_2 production, even using a very low amount as the electrocatalyst [73].

Influence of pH

Evaluation was made of the influence of pH on the amounts of methanol and ethanol generated. For all the electrodes tested, pH 6.4 provided higher photoconversion efficiency for formation of both alcohols, compared to acid and alkaline media (Figure 8). At pH 3.0, the S08 material provided around 1.06x and 1.39x higher methanol generation, compared to S02 and S01, respectively. For ethanol, S02 provided 2.01x and 1.08x higher productivity, compared to S01 and S08. At this pH, the competitive reactions for the active sites of the catalyst were evidenced mainly by the high levels of H^+ ions. Hence, the low performance could be attributed to the generation of H_2 being favored over the reduction of CO_2. At pH 9.0, S08 again showed slightly higher methanol generation, with a value 1.85x and 1.05x higher than obtained using S01 and S02, respectively. Ethanol generation was favored using S02, with a value 3.22x and 1.44x higher than obtained using S01 and S08, respectively. In this medium, the formation of carbonate ions was favored, decreasing the free CO_2 available for the reaction. At the same time, the high pH would shift the composition of the copper particles to copper hydroxide, altering the photocatalytic properties and decreasing the process efficiency.

The pH is extremely important in CO_2 reduction processes, due to the need to suppress the hydrogen evolution reaction [72,74,75]. Pronounced effects on the behavior can occur due to changes of the residual functional groups present on the GNRs, such as carboxyl [15,31,50,54,76], hydroxyl, carbonyl, and ether groups [31,50,54]. Protonation and deprotonation reactions of the groups at the edges of the GNRs, under different pH conditions, can be exploited to tune the electrostatic interactions. Deprotonation reactions are predominant when higher pH values are used, resulting in a negatively charged structure, due to several of the groups present at the edges of the GNRs. However, at lower pH values, the protonation of these groups results in considerable increases in Van der Waals or p-p bond type interactions between the GNR sheets, leading to lower availability of active sites for CO_2 coordination [15,24,31–33,76,77]. The results showed that the CO_2 reduction became more favorable at pH 6.4, compared to the other conditions, due to less competition for the GNR active sites. The best performance for the generation of methanol was obtained using S01, which provided values 1.41x and 1.76x higher than obtained using S02 and S08, respectively. For ethanol, S02 was the most favorable material, with a value 5.04x and 1.34x higher than obtained with S01 and S08, respectively. Minimization of the competitive processes resulted in increased interaction of CO_2 with the catalyst surface, consequently increasing the formation of the desired products.

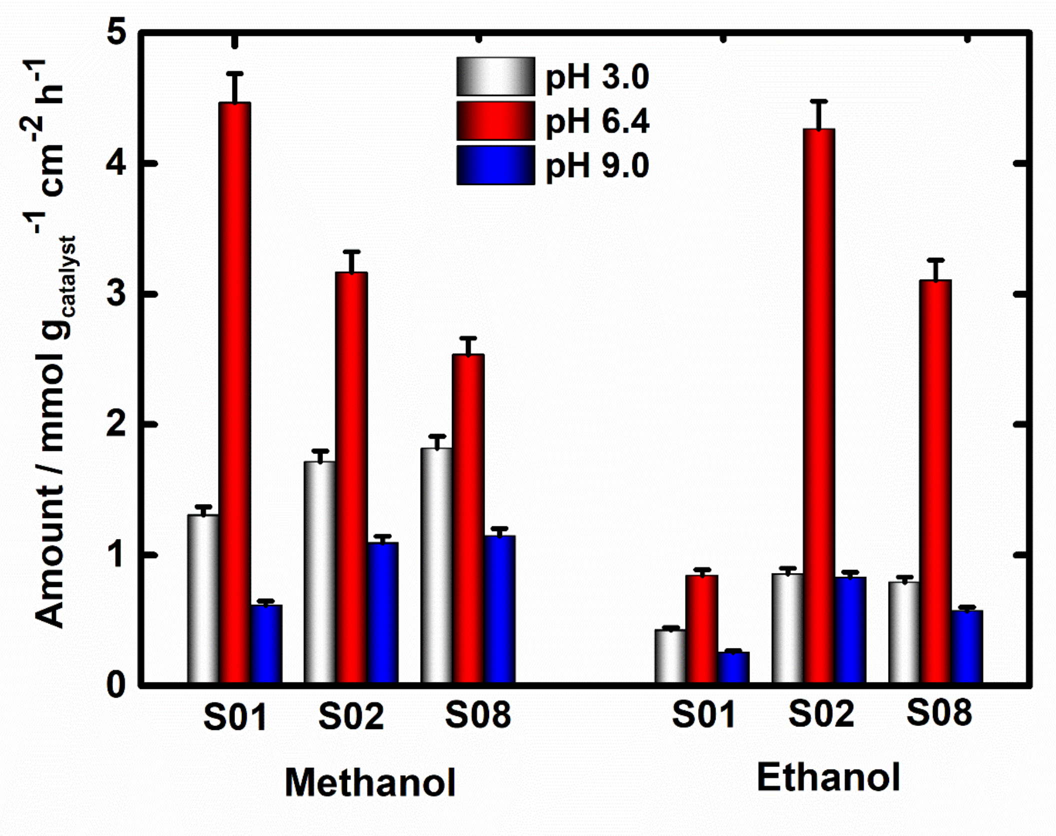

Figure 8. Amounts of methanol and ethanol generated in the photoelectrocatalytic processes performed using the S01, S02, and S08 electrodes for 1 h at pH 3.0 (white columns), pH 6.4 (red columns), and pH 9.0 (blue columns), with bias potential of -0.7 V vs. Ag/AgCl, in 0.1 mol L^{-1} Na_2SO_4, under illumination from a 150 W xenon lamp.

Influence of bias potential

The effect of the bias potential (-0.7 V, +0.1 V, and +1.0 V vs. Ag/AgCl (3.0 mol L^{-1} KCl)) on the photoelectrocatalytic reduction of CO_2 is shown in Figure 9.

The application of a potential of -0.7 V was only favorable for the generation of methanol using the S01 electrode, with values 1.41x and 1.76x higher than obtained with the S02 and S08 electrodes, respectively. For the generation of ethanol, the S02 electrode provided the best response, with a value 4.93x and 1.25x higher than achieved with the S01 and S08 electrodes, respectively. For E_{bias} of +0.1 V, the greatest formation of methanol and ethanol was found for the S08 electrode, which provided a value for methanol that was 1.42x and 1.80x higher than using S01 and S02, respectively, while the value for ethanol was 2.61x and 2.72x higher than obtained using the S01 and S02 electrodes, respectively. The highest amounts of both alcohols were obtained when E_{bias} of +1.0 V was applied with the S02 electrode. This resulted in a methanol value that was 2.25x and 1.89x higher than obtained with S01 and S08, respectively, while the value for ethanol was 3.81x and 2.28x higher than achieved with the S01 and S08 electrodes, respectively.

These effects may have been related to some changes in the properties of the materials, such as the oxidation of copper nanoparticles that are among the main agents responsible for the generation of hydrocarbons and carbonaceous compounds. Another important factor is the attraction of electrons by metal nanoparticles. These two factors may contribute to the CO_2 reduction process either individually or in combination. According to the linear voltammograms (Fig. 5), at positive potentials (+0.1 and +1.0 V), the photocurrents obtained were in the middle and stabilized on a plateau, respectively. When an external potential is applied, some carriers are forced to move or attempt to move through the depletion region and are scavenged to the surface, due to electrostatic forces exerted by the metallic particles [33,41]. In this situation, materials with a greater amount of metallic particles will promote more intense attraction in their direction, consequently increasing the possibility of reaction with the adsorbed CO_2. This was evidenced by the performance shown by the S02 catalyst, although it should be noted that reactions leading to H_2 generation might compete with CO_2 reduction. Hence, materials able to promote higher generation of charge carriers (electrons), which are attracted more rapidly to the surface of the material, are more efficient in promoting the CO_2 reduction reactions [15,24,33].

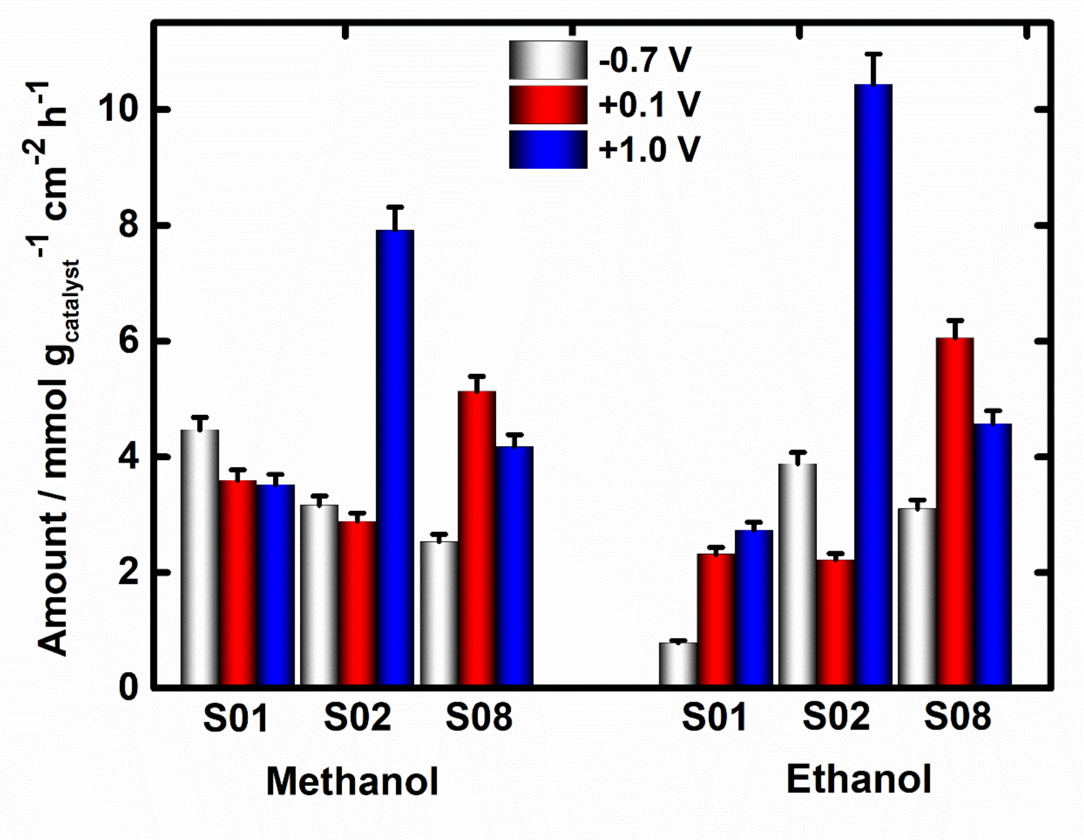

Figure 9. Amounts of methanol and ethanol generated in the photoelectrocatalytic processes performed using the S01, S02, and, S08 electrodes for 1 h, at bias potentials of -0.7 V (white columns), +0.1 V (red columns), and +1.0 V (blue columns) vs. Ag/AgCl, in 0.1 mol L^{-1} Na_2SO_4, at pH 6.4, under illumination from a 150 W xenon lamp.

CO_2 reduction using different techniques

A performance comparison for CO_2 reduction was performed using the S01, S02, and S08 materials in photoelectrocatalysis (PEC: bias potential (1.0 V vs. Ag/AgCl (3.0 mol L^{-1} KCl)) + photocatalyst + light), photocatalysis (PC: photocatalyst + light), photolysis (PT: only light), and electrocatalysis (EC: bias potential (1.0 V vs. Ag/AgCl (3.0 mol L^{-1} KCl)). The amounts of methanol and ethanol formed after 60 min are shown in Figure 10.

In the PT experiments, no products were observed after 60 min, which could be explained by the inability of the energy of the radiation emitted by the photolysis lighting system to spontaneously convert CO_2 into alcohols. For the EC process, the absence of products could be attributed to the need to activate the photocatalyst using a light energy greater than or equal to the band gap, in order to promote the generation of charge carriers responsible for reducing CO_2. In the PEC process, higher values were obtained for methanol and ethanol generation, compared to the PC process, showing that the application of potential in the photoelectrocatalytic system was effective in improving the performance of the system. The main explanation for this was the better use of photogenerated electrons and fast electronic transfer to the surface of the catalyst, favored by the band bending and minimization of charge recombination [15,24,67]. Furthermore, the assembly of the TiO_2-NT/GNR-M system greatly favored the transfer of electrons to the surface of the catalyst, efficiently promoting reduction of the CO_2 adsorbed on its surface. In this configuration, the effects of the metals together on the GNRs minimized the reactions leading to generation of H_2, enabling the formation of both alcohols simultaneously and in large amounts, with faradic efficiencies calculated for methanol and ethanol, respectively around: S01 in 84.17% and 13.78%, for S02 in 59.66% and 17.91% and S08 in 51.22% and 8.83%.

The stability of each material was evaluated after 15 h of experiment. After this period, part of the catalyst deposited on the surface of the TiO_2-NT was leached, leaving the nanotubes exposed. The monitoring was accompanied through the current transient analyzes, performing the preparation of a new TiO_2-NT/GNR-M plate after a decay of the current of 20% of the original value. As a consequence, reductions in the amounts of methanol and ethanol formed were observed for longer times. This behavior could be explained by oxidation of the products by the holes and/or hydroxyl radicals generated at the surface without the GNR-metal.

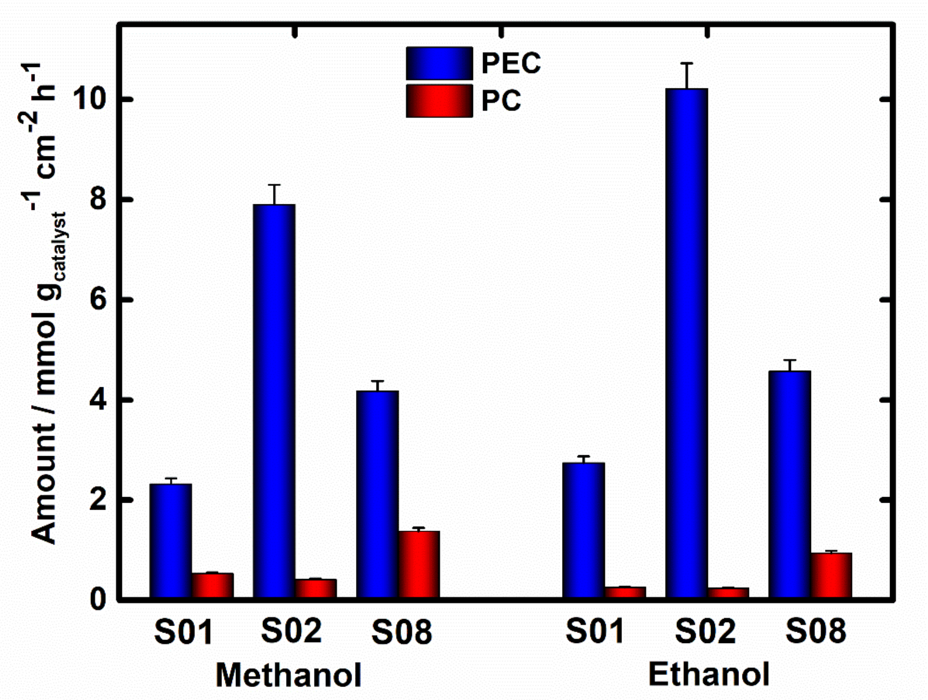

Figure 10. Amounts of methanol and ethanol generated using the S01, S02, and S08 electrodes for 1 h in the photoelectrocatalysis (blue columns) and photocatalysis (red

columns) techniques, with bias potentials of 1.0 V vs. Ag/AgCl, in 0.1 mol L^{-1} Na_2SO_4, at pH 6.4, under illumination from a 150 W xenon lamp.

Conclusions

The assembly of TiO_2-NT photocatalysts containing graphene nanoribbons with the metals Cu, Pd, and Pt in different proportions proved to be very effective in promoting the photoelectrocatalytic reduction of CO_2 to methanol and ethanol. Under optimized conditions, the S01, S02, and S08 materials were effective for this photoelectroconversion, especially when using smaller amounts of metals (~2.5 wt.%, 3.8 μg cm^{-2} of Cu, Pd, and Pt). This strategy enabled significant quantities of methanol and ethanol to be produced, due to better use of photogenerated electrons, minimization of charge recombination processes, and avoidance of reactions leading to H_2 generation.

Acknowledgments

The authors are grateful for the financial support provided by the Brazilian funding agencies FAPESP (#2015/18109-4; #2017/10118-0; #2019/04421-7; #2014/50945-1 INCT-DATREM), CNPq (#303759/2014-3, #409792/2018-7, #303351/2018-7, and #405742/2018-5), Fundect-MS (#23/200.246/2014 and #59/300.184/2016), and CAPES (PNPD and Finance Code 001). Authors also acknowledge the Laboratory of Structural Characterization (LCE/DEMa/UFSCar) for the TEM facilities.

References

[1] C. Ampelli, C. Genovese, R. Passalacqua, S. Perathoner, G. Centi, The use of a solar photoelectrochemical reactor for sustainable production of energy, Theor. Found. Chem. Eng. 46 (2012) 651–657. https://doi.org/10.1134/S0040579512060012.

[2] O. Ola, M.M. Maroto-Valer, Review of material design and reactor engineering on TiO2 photocatalysis for CO2 reduction, J. Photochem. Photobiol. C Photochem. Rev. 24 (2015) 16–42. https://doi.org/10.1016/j.jphotochemrev.2015.06.001.

[3] D. R. Sauerbeck, CO2 emissions and C sequestration by agriculture - perspecives and limitations, Nutr. Cycl. Agroecosystems. 60 (2001) 253–266. https://doi.org/10.1007/BF01105009.

[4] M.J.W. Blom, W.P.M. van Swaaij, G. Mul, S.R.A. Kersten, Overall mass balance

evaluation of electrochemical reactors: The case of CO2 reduction, Electrochim. Acta. 333 (2020) 135460. https://doi.org/10.1016/j.electacta.2019.135460.

[5] F. Zhang, C. Chen, Y. Tang, Z. Cheng, CO2 reduction in a microchannel electrochemical reactor with gas-liquid segmented flow, Chem. Eng. J. 392 (2020) 124798. https://doi.org/10.1016/j.cej.2020.124798.

[6] A.A. Khan, M. Tahir, Recent advancements in engineering approach towards design of photo-reactors for selective photocatalytic CO2 reduction to renewable fuels, J. CO2 Util. 29 (2019) 205–239. https://doi.org/10.1016/j.jcou.2018.12.008.

[7] M. Tahir, N.S. Amin, Advances in visible light responsive titanium oxide-based photocatalysts for CO2 conversion to hydrocarbon fuels, Energy Convers. Manag. 76 (2013) 194–214. https://doi.org/10.1016/j.enconman.2013.07.046.

[8] M. Flores-Flores, E. Luévano-Hipólito, L.M. Torres-Martínez, T.O. Do, CO2 adsorption and photocatalytic reduction over Mg(OH)2 /CuO/Cu2O under UV-Visible light to solar fuels, Mater. Chem. Phys. 227 (2019) 90–97. https://doi.org/10.1016/j.matchemphys.2019.01.062.

[9] G.G. Bessegato, T.T. Guaraldo, J.F. de Brito, M.F. Brugnera, M.V.B. Zanoni, Achievements and Trends in Photoelectrocatalysis: from Environmental to Energy Applications, Electrocatalysis. 6 (2015) 415–441. https://doi.org/10.1007/s12678-015-0259-9.

[10] K. Rajeshwar, N.R. De Tacconi, G. Ghadimkhani, W. Chanmanee, C. Janáky, Tailoring copper oxide semiconductor nanorod arrays for photoelectrochemical reduction of carbon dioxide to methanol, ChemPhysChem. 14 (2013) 2251–2259. https://doi.org/10.1002/cphc.201300080.

[11] O.K. Varghese, M. Paulose, T.J. LaTempa, C.A. Grimes, High-Rate Solar Photocatalytic Conversion of CO_2 and Water Vapor to Hydrocarbon Fuels, Nano Lett. 9 (2009) 731–737. https://doi.org/10.1021/nl803258p.

[12] J.-R. Li, Y. Ma, M.C. McCarthy, J. Sculley, J. Yu, H.-K. Jeong, P.B. Balbuena, H.-C. Zhou, Carbon dioxide capture-related gas adsorption and separation in metal-organic frameworks, Coord. Chem. Rev. 255 (2011) 1791–1823. https://doi.org/10.1016/j.ccr.2011.02.012.

[13] N. Yang, S.R. Waldvogel, X. Jiang, Electrochemistry of Carbon Dioxide on Carbon Electrodes, ACS Appl. Mater. Interfaces. 8 (2016) 28357–28371. https://doi.org/10.1021/acsami.5b09825.

[14] J. Bugayong, G.L. Griffin, Electrochemical Reduction of CO2 using Supported Cu2O Catalysts, MRS Proc. 1542 (2013) mrss13-1542-g05-11. https://doi.org/10.1557/opl.2013.833.

[15] A. García, C. Fernandez-Blanco, J.R. Herance, J. Albero, H. García, Graphenes as additives in photoelectrocatalysis, J. Mater. Chem. A. 5 (2017) 16522–16536. https://doi.org/10.1039/c7ta04045h.

[16] Q. Lu, F. Jiao, Electrochemical CO2 reduction: Electrocatalyst, reaction mechanism, and process engineering, Nano Energy. 29 (2016) 439–456. https://doi.org/10.1016/j.nanoen.2016.04.009.

[17] A.M. Qadir, I.Y. Erdogan, Structural properties and enhanced photoelectrochemical performance of ZnO films decorated with Cu2O nanocubes, Int. J. Hydrogen Energy. (2019) 1–9. https://doi.org/10.1016/j.ijhydene.2019.01.101.

[18] J.B. Vennekoetter, R. Sengpiel, M. Wessling, Beyond the catalyst: How electrode and reactor design determine the product spectrum during electrochemical CO2 reduction, Chem. Eng. J. 364 (2019) 89–101. https://doi.org/10.1016/j.cej.2019.01.045.

[19] M. Pelaez, N. Nolan, S. Pillai, M. Seery, P. Falaras, A Review on the Visible Light Active Titanium Dioxide Photocatalysts for Environmental Applications, Appl. Catal. BEnvironmental. 12505 (2012) 331–349. https://doi.org/10.1016/j.apcatb.2012.05.036.

[20] T. Kulandaivalu, S. Abdul Rashid, N. Sabli, T.L. Tan, Visible light assisted photocatalytic reduction of CO2 to ethane using CQDs/Cu2O nanocomposite photocatalyst, Diam. Relat. Mater. 91 (2019) 64–73. https://doi.org/10.1016/j.diamond.2018.11.002.

[21] W. Dai, H. Xu, J. Yu, X. Hu, X. Luo, X. Tu, L. Yang, Photocatalytic reduction of CO2 into methanol and ethanol over conducting polymers modified Bi2WO6 microspheres under visible light, Appl. Surf. Sci. 356 (2015) 173–180. https://doi.org/10.1016/j.apsusc.2015.08.059.

[22] S. Sato, T. Arai, T. Morikawa, K. Uemura, T.M. Suzuki, H. Tanaka, T. Kajino, Selective CO2 Conversion to Formate Conjugated with H2O Oxidation Utilizing Semiconductor/Complex Hybrid Photocatalysts, J. Am. Chem. Soc. 133 (2011) 15240–15243. https://doi.org/10.1021/ja204881d.

[23] S. Das, W.M.A.W. Daud, Photocatalytic CO2 transformation into fuel: A review

on advances in photocatalyst and photoreactor, 39 (2014) 765–805. https://doi.org/10.1039/c4ra01769b.

[24] B. Adeli, F. Taghipour, Role of Graphene in Photocatalytic Solar Fuel Generation, Visible-Light Photocatal. Carbon-Based Mater. (2018). https://doi.org/10.5772/intechopen.72623.

[25] C. Janáky, K. Rajeshwar, The role of (photo)electrochemistry in the rational design of hybrid conducting polymer/semiconductor assemblies: From fundamental concepts to practical applications, Prog. Polym. Sci. 43 (2015) 96–135. https://doi.org/10.1016/j.progpolymsci.2014.10.003.

[26] D. Zhang, B. Hu, D. Guan, Z. Luo, Essential roles of defects in pure graphene/Cu2O photocatalyst, Catal. Commun. 76 (2016) 7–12. https://doi.org/10.1016/j.catcom.2015.12.013.

[27] G. Zhu, Y. Li, H. Zhu, H. Su, S.H. Chan, Q. Sun, Enhanced CO2 electroreduction on armchair graphene nanoribbons edge-decorated with copper, Nano Res. 10 (2017) 1641–1650. https://doi.org/10.1007/s12274-016-1362-9.

[28] K. Li, X. An, K.H. Park, M. Khraisheh, J. Tang, A critical review of CO2 photoconversion: Catalysts and reactors, Catal. Today. 224 (2014) 3–12. https://doi.org/10.1016/j.cattod.2013.12.006.

[29] M. Xing, F. Shen, B. Qiu, J. Zhang, Highly-dispersed Boron-doped graphene nanosheets loaded with TiO 2 nanoparticles for enhancing CO2 photoreduction, Sci. Rep. 4 (2014) 1–7. https://doi.org/10.1038/srep06341.

[30] C. Rogers, W.S. Perkins, G. Veber, T.E. Williams, R.R. Cloke, F.R. Fischer, Synergistic Enhancement of Electrocatalytic CO2 Reduction with Gold Nanoparticles Embedded in Functional Graphene Nanoribbon Composite Electrodes, J. Am. Chem. Soc. 139 (2017) 4052–4061. https://doi.org/10.1021/jacs.6b12217.

[31] F. De Lima, G. Maia, Oxidized/reduced graphene nanoribbons facilitate charge transfer to the Fe(CN)63-/Fe(CN)64- redox couple and towards oxygen reduction, Nanoscale. 7 (2015) 6193–6207. https://doi.org/10.1039/c5nr01123j.

[32] C. V. Boone, G. Maia, Lowering metal loadings onto Pt–Pd–Cu/graphene nanoribbon nanocomposites affects electrode collection efficiency and oxygen reduction reaction performance, Electrochim. Acta. 303 (2019) 192–203. https://doi.org/10.1016/j.electacta.2019.02.079.

[33] L.Y. Ozer, C. Garlisi, H. Oladipo, M. Pagliaro, S.A. Sharief, A. Yusuf, S.

Almheiri, G. Palmisano, Inorganic semiconductors-graphene composites in photo(electro)catalysis: Synthetic strategies, interaction mechanisms and applications, J. Photochem. Photobiol. C Photochem. Rev. 33 (2017) 132–164. https://doi.org/10.1016/j.jphotochemrev.2017.06.003.

[34] K. Zhou, Y. Zhu, X. Yang, X. Jiang, C. Li, Preparation of graphene-TiO2 composites with enhanced photocatalytic activity, New J. Chem. 35 (2011) 353–359. https://doi.org/10.1039/c0nj00623h.

[35] M.R. Hasan, S.B. Abd Hamid, W.J. Basirun, S.H. Meriam Suhaimy, A.N. Che Mat, A sol-gel derived, copper-doped, titanium dioxide-reduced graphene oxide nanocomposite electrode for the photoelectrocatalytic reduction of CO2 to methanol and formic acid, RSC Adv. 5 (2015) 77803–77813. https://doi.org/10.1039/c5ra12525a.

[36] J. Cheng, M. Zhang, J. Liu, J. Zhou, K. Cen, A Cu foam cathode used as a Pt-RGO catalyst matrix to improve CO2 reduction in a photoelectrocatalytic cell with a TiO2 photoanode, J. Mater. Chem. A. 3 (2015) 12947–12957. https://doi.org/10.1039/c5ta03026a.

[37] X. Li, Q. Wang, Y. Zhao, W. Wu, J. Chen, H. Meng, Green synthesis and photo-catalytic performances for ZnO-reduced graphene oxide nanocomposites, J. Colloid Interface Sci. 411 (2013) 69–75. https://doi.org/10.1016/j.jcis.2013.08.050.

[38] V.C. Hoang, V.G. Gomes, N. Kornienko, Metal-based nanomaterials for efficient CO2 electroreduction: Recent advances in mechanism, material design and selectivity, Nano Energy. 78 (2020) 105311. https://doi.org/10.1016/j.nanoen.2020.105311.

[39] Y. Li, S. Guo, Noble metal-based 1D and 2D electrocatalytic nanomaterials: Recent progress, challenges and perspectives, Nano Today. 28 (2019) 100774. https://doi.org/10.1016/j.nantod.2019.100774.

[40] C. Wang, D. Astruc, Recent developments of metallic nanoparticle-graphene nanocatalysts, Prog. Mater. Sci. 94 (2018) 306–383. https://doi.org/10.1016/j.pmatsci.2018.01.003.

[41] X. Li, J. Yu, M. Jaroniec, X. Chen, Cocatalysts for selective photoreduction of CO2 into solar fuels, Chem. Rev. 119 (2019) 3962–4179. https://doi.org/10.1021/acs.chemrev.8b00400.

[42] T. Wang, M. Park, Q. Yu, J. Zhang, Y. Yang, Stability and synthesis of 2D

metals and alloys: a review, Mater. Today Adv. 8 (2020) 100092. https://doi.org/10.1016/j.mtadv.2020.100092.

[43] J.C. Cardoso, M.V. Boldrin Zanoni, Structural Effects of Nanotubes, Nanowires, and Nanoporous Ti/TiO 2 Electrodes on Photoelectrocatalytic Oxidation of 4,4-Oxydianiline, Sep. Sci. Technol. 45 (2010) 1628–1636. https://doi.org/10.1080/01496395.2010.487721.

[44] J.C. Cardoso, N. Lucchiari, M.V.B. Zanoni, Bubble annular photoeletrocatalytic reactor with TiO2 nanotubes arrays applied in the textile wastewater, J. Environ. Chem. Eng. 3 (2015) 1177–1184. https://doi.org/10.1016/j.jece.2015.04.010.

[45] J.C. Cardoso, T.M. Lizier, M.V.B. Zanoni, Highly ordered TiO2 nanotube arrays and photoelectrocatalytic oxidation of aromatic amine, Appl. Catal. B Environ. 99 (2010) 96–102. https://doi.org/10.1016/j.apcatb.2010.06.005.

[46] F.A. Sayão, J.B. da Silva Flor, R.C.G. Frem, S. Stulp, J.C. Cardoso, M.V.B. Zanoni, Nitrite Reduction Enhancement on Semiconducting Electrode Decorated with Copper(II) Aspirinate Complex, Electrocatalysis. 7 (2016). https://doi.org/10.1007/s12678-016-0327-9.

[47] J.L. Esbenshade, J.C. Cardoso, M.V.B. Zanoni, Removal of sunscreen compounds from swimming pool water using self-organized TiO2 nanotubular array electrodes, J. Photochem. Photobiol. A Chem. 214 (2010) 257–263. https://doi.org/10.1016/j.jphotochem.2010.07.005.

[48] J.C. Cardoso, S. Stulp, J.F. de Brito, J.B.S. Flor, R.C.G. Frem, M.V.B. Zanoni, MOFs based on ZIF-8 deposited on TiO2 nanotubes increase the surface adsorption of CO2 and its photoelectrocatalytic reduction to alcohols in aqueous media, Appl. Catal. B Environ. 225 (2018) 563–573. https://doi.org/10.1016/j.apcatb.2017.12.013.

[49] J.H. Scofield, Hartree-Slater subshell photoionization cross-sections at 1254 and 1487 eV, J. Electron Spectros. Relat. Phenomena. 8 (1976) 129–137. https://doi.org/10.1016/0368-2048(76)80015-1.

[50] C. V. Boone, G. Maia, Pt–Pd and Pt–Pd–(Cu or Fe or Co)/graphene nanoribbon nanocomposites as efficient catalysts toward the oxygen reduction reaction, Electrochim. Acta. 247 (2017) 19–29. https://doi.org/10.1016/j.electacta.2017.06.160.

[51] L.B. Venarusso, J. Bettini, G. Maia, Catalysts for oxygen reduction reaction based on nanocrystals of a Pt or Pt–Pd alloy shell supported on a Au core, J.

Solid State Electrochem. 20 (2016) 1753–1764. https://doi.org/10.1007/s10008-016-3181-z.

[52] L.B. Venarusso, J. Bettini, G. Maia, Superior Catalysts for Oxygen Reduction Reaction Based on Porous Nanostars of a Pt, Pd, or Pt-Pd Alloy Shell Supported on a Gold Core, ChemElectroChem. 3 (2016) 749–756. https://doi.org/10.1002/celc.201600046.

[53] F. Franco, C. Rettenmaier, H.S. Jeon, B. Roldan Cuenya, Transition metal-based catalysts for the electrochemical CO 2 reduction: from atoms and molecules to nanostructured materials, Chem. Soc. Rev. 49 (2020) 6884–6946. https://doi.org/10.1039/D0CS00835D.

[54] E.S.F. Cardoso, G. V. Fortunato, G. Maia, Use of Rotating Ring-Disk Electrodes to Investigate Graphene Nanoribbon Loadings for the Oxygen Reduction Reaction in Alkaline Medium, ChemElectroChem. 5 (2018) 1691–1701. https://doi.org/10.1002/celc.201800331.

[55] E.S.F. Cardoso, G. V. Fortunato, G. Maia, Modification of C, O, and N Groups for Oxygen Reduction Reaction on an Electrochemically Stabilized Graphene Nanoribbon Surface, J. Phys. Chem. C. 123 (2019) 16308–16316. https://doi.org/10.1021/acs.jpcc.9b04422.

[56] G. V. Fortunato, E. Pizzutilo, E.S.F. Cardoso, M.R.V. Lanza, I. Katsounaros, S.J. Freakley, K.J.J. Mayrhofer, G. Maia, M. Ledendecker, The oxygen reduction reaction on palladium with low metal loadings: The effects of chlorides on the stability and activity towards hydrogen peroxide, J. Catal. 389 (2020) 400–408. https://doi.org/10.1016/j.jcat.2020.06.019.

[57] A. FUJISHIMA, X. ZHANG, D. TRYK, TiO2 photocatalysis and related surface phenomena, Surf. Sci. Rep. 63 (2008) 515–582. https://doi.org/10.1016/j.surfrep.2008.10.001.

[58] C.A. Grimes, G.K. Mor, TiO2 nanotube arrays: Synthesis, Properties, and Applications, Springer, New York, 2009. https://doi.org/10.1007/978-1-4419-0068-5.

[59] S.H. Lee, I. Sullivan, D.M. Larson, G. Liu, F.M. Toma, C. Xiang, W.S. Drisdell, Correlating Oxidation State and Surface Area to Activity from Operando Studies of Copper CO Electroreduction Catalysts in a Gas-Fed Device, ACS Catal. 10 (2020) 8000–8011. https://doi.org/10.1021/acscatal.0c01670.

[60] A. Primo, I. Esteve-Adell, J.F. Blandez, A. Dhakshinamoorthy, M. Álvaro, N.

Candu, S.M. Coman, V.I. Parvulescu, H. García, High catalytic activity of oriented 2.0.0 copper(I) oxide grown on graphene film, Nat. Commun. 6 (2015) 8561. https://doi.org/10.1038/ncomms9561.

[61] T.J. Richardson, J.L. Slack, M.D. Rubin, Electrochromism in copper oxide thin films, Electrochim. Acta. 46 (2001) 2281–2284. https://doi.org/10.1016/S0013-4686(01)00397-8.

[62] S. Ohya, S. Kaneco, H. Katsumata, T. Suzuki, K. Ohta, Electrochemical reduction of CO2 in methanol with aid of CuO and Cu2O, Catal. Today. 148 (2009) 329–334. https://doi.org/10.1016/j.cattod.2009.07.077.

[63] Y. Yang, D. Xu, Q. Wu, P. Diao, Cu2O/CuO bilayered composite as a high-efficiency photocathode for photoelectrochemical hydrogen evolution reaction, Sci. Rep. 6 (2016) 1–13. https://doi.org/10.1038/srep35158.

[64] V. Kumaravel, J. Bartlett, S.C. Pillai, Photoelectrochemical Conversion of Carbon Dioxide (CO2) into Fuels and Value-Added Products, ACS Energy Lett. 5 (2020) 486–519. https://doi.org/10.1021/acsenergylett.9b02585.

[65] X. Chang, T. Wang, P. Yang, G. Zhang, J. Gong, The Development of Cocatalysts for Photoelectrochemical CO2 Reduction, Adv. Mater. 31 (2019) 1–13. https://doi.org/10.1002/adma.201804710.

[66] G.G. Bessegato, T.T. Guaraldo, M.V.B. Zanoni, Enhancement of Photoelectrocatalysis Efficiency by Using Nanostructured Electrodes, in: Mod. Electrochem. Methods Nano, Surf. Corros. Sci., InTech, 2014: pp. 271–319. https://doi.org/10.5772/57202.

[67] G. Zhao, X. Huang, X. Wang, X. Wang, Progress in catalyst exploration for heterogeneous CO2 reduction and utilization: A critical review, J. Mater. Chem. A. 5 (2017) 21625–21649. https://doi.org/10.1039/c7ta07290b.

[68] C. Maeda, Y. Miyazaki, T. Ema, Recent progress in catalytic conversions of carbon dioxide, Catal. Sci. Technol.,. 4 (2014) 1482–1497. https://doi.org/10.1039/c3cy00993a.

[69] R.P.S. Chaplin, A.A. Wragg, Effects of process conditions and electrode material on reaction pathways for carbon dioxide electroreduction with particular reference to formate formation, J. Appl. Electrochem. 33 (2003) 1107–1123. https://doi.org/10.1023/B:JACH.0000004018.57792.b8.

[70] R. Kortlever, J. Shen, K.J.P. Schouten, F. Calle-Vallejo, M.T.M. Koper, Catalysts and Reaction Pathways for the Electrochemical Reduction of Carbon

Dioxide, J. Phys. Chem. Lett. 6 (2015) 4073–4082. https://doi.org/10.1021/acs.jpclett.5b01559.

[71] R.K. Derichter, T. Ming, S. Caillol, Fighting global warming by photocatalytic reduction of CO2 using giant photocatalytic reactors, Renew. Sustain. Energy Rev. 19 (2013) 82–106. https://doi.org/10.1016/j.rser.2012.10.026.

[72] M.R. Singh, E.L. Clark, A.T. Bell, Effects of electrolyte, catalyst, and membrane composition and operating conditions on the performance of solar-driven electrochemical reduction of carbon dioxide., Phys. Chem. Chem. Phys. 17 (2015) 18924–36. https://doi.org/10.1039/c5cp03283k.

[73] J. Theerthagiri, E.S.F. Cardoso, G. V. Fortunato, G.A. Casagrande, B. Senthilkumar, J. Madhavan, G. Maia, Highly Electroactive Ni Pyrophosphate/Pt Catalyst toward Hydrogen Evolution Reaction, ACS Appl. Mater. Interfaces. 11 (2019) 4969–4982. https://doi.org/10.1021/acsami.8b18153.

[74] Y.E. Shin, Y.J. Sa, S. Park, J. Lee, K.H. Shin, S.H. Joo, H. Ko, An ice-templated, pH-tunable self-assembly route to hierarchically porous graphene nanoscroll networks, Nanoscale. 6 (2014) 9734–9741. https://doi.org/10.1039/c4nr01988a.

[75] D. Li, M.B. Müller, S. Gilje, R.B. Kaner, G.G. Wallace, Processable aqueous dispersions of graphene nanosheets, Nat. Nanotechnol. 3 (2008) 101–105. https://doi.org/10.1038/nnano.2007.451.

[76] J. Liu, Y. Niu, X. He, J. Qi, X. Li, Photocatalytic reduction of CO2 Using TiO2-graphene nanocomposites, J. Nanomater. 2016 (2016) 3–8. https://doi.org/10.1155/2016/6012896.

[77] P. Yang, S. Guo, X. Yu, F. Zhang, B. Yu, H. Zhang, Y. Zhao, Z. Liu, Photocatalytic Reduction of Carbon Dioxide over Quinacridone Nanoparticles Supported on Reduced Graphene Oxide, Ind. Eng. Chem. Res. 58 (2019) 9636–9643. https://doi.org/10.1021/acs.iecr.9b00242.

Figure captions

Figure 1. Representative BF-STEM (first row), TEM (second row), and HR-TEM (third and four rows) images for the S01, S02, and S08 samples.

Figure 2. Scanning electron microscopy images of samples S01, S02, S08, and S07, using (A) secondary electron mode (SEI) and (B) backscattered electron mode (BSE). (C) Results of scanning electron microscopy/energy dispersive X-ray spectrometry (SEM/EDX) analyses of the materials.

Figure 3. Thermal decomposition behaviors of (A) S07, (B) S01, (C) S02, and (D) S08.

Figure 4. Absorption spectra as a function of wavelength by DRS analysis of (A) TiO_2 nanotubes, (B) S07, (C) S01, (D) S02, and (E) S08.

Figure 5. Linear scanning voltammograms for the different electrodes: (A) S08 in the dark, (B) TiO_2 nanotubes, (C) S07, (D) S01, (E) S02, and (F) S08. Conditions: $\upsilon = 10$ mV s^{-1}; 0.1 mol L^{-1} Na_2SO_4; pH 6.4; illumination using a 150 W xenon lamp.

Figure 6. Amounts of methanol (blue columns) and ethanol (red columns) generated by the photoelectrocatalytic process using the S01, S02, and S08 electrodes for 1 h, with bias potential of -0.7 V vs. Ag/AgCl, in 0.1 mol L^{-1} Na_2SO_4, at pH 6.4, under illumination from a 150 W xenon lamp.

Figure 7. Proposed scheme for the generation of products using the TiO_2-NT/GNR-metal electrodes operated under UV-Vis irradiation.

Figure 8. Amounts of methanol and ethanol generated in the photoelectrocatalytic processes performed using the S01, S02, and S08 electrodes for 1 h at pH 3.0 (white columns), pH 6.4 (red columns), and pH 9.0 (blue columns), with bias potential of -0.7 V vs. Ag/AgCl, in 0.1 mol L^{-1} Na_2SO_4, under illumination from a 150 W xenon lamp.

Figure 9. Amounts of methanol and ethanol generated in the photoelectrocatalytic processes performed using the S01, S02, and, S08 electrodes for 1 h, at bias potentials of -0.7 V (white columns), +0.1 V (red columns), and +1.0 V (blue columns) vs. Ag/AgCl, in 0.1 mol L^{-1} Na_2SO_4, at pH 6.4, under illumination from a 150 W xenon lamp.

Figure 10. Amounts of methanol and ethanol generated using the S01, S02, and S08 electrodes for 1 h in the photoelectrocatalysis (blue columns) and photocatalysis (red columns) techniques, with bias potentials of 1.0 V vs. Ag/AgCl, in 0.1 mol L^{-1} Na_2SO_4, at pH 6.4, under illumination from a 150 W xenon lamp.

Table caption

Table 1. Experimental values (weight %) obtained for the elemental compositions of the S01, S02, S08, and S07 materials, based on the masses remaining unburned after the TG analyses (Figure 3) and the metals detected in the EDX analyses (Figure 2).

Supplementary Material captions

Table S1. Graphene nanoribbon (GNR), salt, Pluronic F-127, and ascorbic acid masses.

Table S2. Chromatographic conditions for analysis of methanol and ethanol.

Table S3. Amounts of methanol and ethanol generated by photoelectrocatalytic CO_2 reduction using the TiO_2-NT-GNR-M electrodes at -0.7 V vs. Ag/AgCl (3.0 mol L^{-1} KCl), in 0.1 mol L^{-1} Na_2SO_4, at pH 6.4, under illumination from a 150 W xenon lamp. The compounds were determined by gas chromatography with flame ionization detection.

Figure S1. Photoreactor used in all the experiments. (A) 150 W xenon lamp; (B) quartz window; (C) working electrode; (D) reference electrode; (E) counter electrode; (F) septum; (G) manometer; (H) headspace; (I) supporting electrolyte; (J) magnetic bar. Reprinted from ref. [44] (with permission).

Figure S2. Elemental EDX-mapping images for the S08 sample.

Figure S3: XPS spectra for the S01, S02, S07, and S08 samples.

Figure S4. HR-XPS spectra in the C 1s, O 1s, and N 1s regions for the S01, S02, S07, and S08 samples.

Figure S5. HR-XPS spectra in the Ti 2p, Cu 2p, Pt 4f, and Pd 3d regions for the S01, S02, S07, and S08 samples.

Table S4. Positions and percent contents of functional groups in the catalyst samples. Values obtained from high-resolution XPS spectra in Figures S4 and S5.

Table S5. Peaks, positions, relative sensitivity factors (R.S.F.), and percent contents of functional groups in the catalyst samples. Values obtained from survey XPS spectra in Figure S3.

Figure S6. Bandgap analysis by Tauch plot.

Table S6. Detailing to obtain values of each metal from the scanning electron microscopy / energy dispersive X-ray spectrometry technique.